Struct Multidisc Optim (2007) 34:507–524
DOI 10.1007/s00158-007-0105-7

RESEARCH PAPER

Topology optimization of flow domains using the lattice Boltzmann method

Georg Pingen · Anton Evgrafov · Kurt Maute

Received: 5 April 2006 / Revised manuscript received: 20 September 2006 / Published online: 20 March 2007

Abstract We consider the optimal design of two- (2D) and three-dimensional (3D) flow domains using the lattice Boltzmann method (LBM) as an approximation of Navier-Stokes (NS) flows. The problem is solved by a topology optimization approach varying the effective porosity of a fictitious material. The boundaries of the flow domain are represented by potentially discontinuous material distributions. NS flows are traditionally approximated by finite element and finite volume methods. These schemes, while well established as high-fidelity simulation tools using body-fitted meshes, are effected in their accuracy and robustness when regular meshes with zero-velocity constraints along the surface and in the interior of obstacles are used, as is common in topology optimization. Therefore, we study the potential of the LBM for approximating low Mach number incompressible viscous flows for topology optimization. In the LBM the geometry of flow domains is defined in a discontinuous manner, similar to the approach used in material-based topology optimization. In addition, this non-traditional discretization method features parallel scalability and allows for high-resolution, regular fluid meshes. In this paper, we show how the variation of the porosity can be used in conjunction with the LBM for the optimal design of fluid domains, making the LBM an interesting alternative to NS solvers for topology optimization problems. The potential of our topology optimization approach will be illustrated by 2D and 3D numerical examples.

Keywords Navier-Stokes flow · Lattice Boltzmann method · Topology optimization

G. Pingen (✉) · A. Evgrafov · K. Maute
Center for Aerospace Structures, Department of Aerospace Engineering Sciences, University of Colorado, Boulder, CO 80309–0429, USA
e-mail: pingen@colorado.edu

A. Evgrafov
e-mail: antone@colorado.edu

K. Maute
e-mail: maute@colorado.edu

1 Introduction

The optimal control of fluid flows has received considerable attention by engineers and mathematicians, owing to its importance for many technical and scientific applications. The reader is referred to the recent monographs of Gunzburger (2003) and Mohammadi and Pironneau (2001). Traditionally, the geometry of flow domains is optimized by varying the shape of obstacles and/or channel walls. We refer, for example, to the body of work by Jameson (1988) and coworkers on shape optimization for external and internal flows. Shape optimization methods, however, allow varying only the shape of boundaries present in the initial design. This limitation can be overcome by extending and applying the concepts of topology optimization originally developed for design problems in solid mechanics to flow problems. These concepts allow the generation of complex, often nonintuitive optimal geometries and do not require an initial, close to optimum design to start with. We refer to the monograph of Bendsøe and Sigmund (2003) for an overview of topology optimization methods.

While the field of topology optimization is well established for the optimal design of solids and structures, little work has been done on topology optimization

of flow problems. In their pioneering work, Borrvall and Petersson (2003) considered the optimal design of Stokes flow problems by distributing inhomogeneous porous materials with a spatially varying Darcy permeability tensor. This approach was generalized by Evgrafov (2005a) to include both limiting cases of porous materials, i.e., pure solid and pure flow regions are allowed to appear in the design domain as a result of the optimization procedure. The Stokes theory is only valid for flows with a small Reynolds number $\mathrm{Re} < 1$. To overcome this limitation, Gersborg-Hansen et al. (2005) extended the approach of Borrvall and Petersson (2003) to laminar incompressible Navier-Stokes (NS) flows at low Reynolds numbers. Evgrafov (2005b) studied the well-posedness of topology optimization problems for incompressible NS flows in the original infinite-dimensional setting, and proposed to relax the incompressibility constraint, among other modifications, to achieve such a well-posedness.

Internal and external NS flows are typically approximated by finite element and finite volume methods (FVMs). These discretization methods are well established as high-fidelity simulation tools using body-fitted meshes. In particular, for complex three-dimensional (3D) geometries, generating body-fitted meshes is an often cumbersome task and the accuracy and numerical robustness of finite element and finite volume methods strongly depends on the quality of the fluid mesh, in particular, as Reynolds and Mach numbers increase. In contrast to body-fitted mesh approaches, immersed boundary techniques represent the geometry of an obstacle by imposing zero-velocity constraints inside the obstacle and at its surface. At the cost of accuracy, these techniques allow for the use of regular meshes, significantly simplifying the mesh generation and allowing for simple-mesh refinement procedures and fine-tuning of the computational performance of the flow solver. Today's topology optimization approaches are based on a simple but rough immersed boundary technique representing the geometry of obstacles with "0–1" discontinuous material distributions and weakly imposed zero-velocity constraints.

In this study, we adopt an immersed boundary approach for topology optimization purposes. However, instead of finite element or finite volume methods, we propose to simulate the underlying flow problem by the lattice Boltzmann method (LBM), a cellular automata approach for simulating low Mach number incompressible viscous flows with an inherit immersed boundary technique. In contrast to finite element and finite volume schemes, the LBM does not discretize the NS equations but operates on a discrete form of the Boltzmann equations. The geometry of obstacles and channel walls is defined by turning off nodes in typically structured fluid meshes. This approach allows the description of complex geometries without the need for generating fluid meshes aligned with the contours of the flow domain. Transforming this on/off nature of lattice nodes into a continuous process by varying the effective porosity of a fictitious material, we obtain an optimization scheme similar to structural topology optimization. In addition, LBM solvers can be efficiently parallelized allowing for high-resolution fluid meshes. The potential of the LBM has been recently recognized for a broad range of technical applications and for complex biological flow problems. Here, we present a design approach that exploits the unique features of the LBM for topology optimization purposes.

2 Problem statements

In general terms a topology optimization problem can be written as follows:

$$\min_{(\vec{d},\vec{u})} \mathcal{F}(\vec{d},\vec{u}),$$
$$\text{s.t.} \begin{cases} \vec{d}, & \text{subject to design constraints,} \\ \vec{u}, & \text{solves the governing equations for } \vec{d}, \end{cases} \tag{1}$$

where $\mathcal{F}$ is a particular performance functional (objective), $\vec{d}$ is the vector of design variables, and $\vec{u}$ is the corresponding state vector.

Borrvall and Petersson (2003) modified the NS equations to include a design variable, leading essentially to the Brinkman or Darcy-Stokes equations, which describe a flow of viscous fluid through a porous medium (Brinkmann 1947; Allaire 1990). In the current work we show that the use of the lattice Boltzmann equation as the governing equation leads to comparable results and can result in several computational advantages. In the current section we therefore first discuss the LBM, then its application to topology optimization, and finally we compare the lattice Boltzmann approach to the original NS approach used by Borrvall and Petersson (2003).

2.1 The lattice Boltzmann method

In recent years, the LBM has become a popular alternative to conventional, NS-based computational methods for a variety of problems in fluid dynamics. The reader is referred to McNamara and Zanetti (1988), Succi (2001), Chen and Doolen (1998), Lou (2000), Wolf-Gladrow (2000), and Dupuis (2002) for an introduction into LBM schemes and applications.

Breuer et al. (2000), He and Doolen (1997a,b), and Hou et al. (1994) have successfully compared the LBM to a number of NS-based finite element, finite difference, and finite-volume methods. Inamuro et al. (1997) and Mei et al. (2002) have compared the LBM to analytical solutions of the NS equations. With respect to applications, the LBM is particularly suited for the solution of problems with complex geometries due to its inherent use of immersed boundary techniques. It has been primarily used to numerically approximate low Mach number flows for a wide array of applications (see, for example, Krafczyk 2001; Succi 2001; Hoekstra et al. 2004).

The LBM was originally derived as an extension of the lattice gas automaton. For information on the lattice gas automata, see, for example, Frisch et al. (1986, 1987) and Rothman and Zaleski (1994). It can also be directly derived from the Boltzmann equation, or the Boltzmann equation with the Bhatnagar-Gross-Krook (BGK) collision operator (Bhatnagar et al. 1954; He and Lou 1997a; Abe 1997). The Boltzmann equation is based on the kinetic theory of gases and it describes the statistical interaction of particles on the molecular level. In contrast, the LBM is based on a single-particle distribution function, which represents an ensemble average of the individual particles, whose behavior is modeled by the Boltzmann equation, thus reducing the number of equations needed to model a fluid while still capturing the physics of microscopic and mesoscopic processes in the fluid. Some of the foundational work on the LBM is discussed by McNamara and Zanetti (1988), Higuera and Jiminez (1989) Higuera et al. (1989) Koelman (1991) Qian et al. (1992), and Chen and Doolen (1998).

The numerical scheme of the LBM can be derived starting with the Boltzmann-BGK equation as shown by Yu et al. (2005):

$$\frac{\partial f}{\partial t} + \xi \cdot \nabla f = -\frac{1}{\lambda}(f - f^{\mathrm{eq}}), \tag{2}$$

where f is the distribution function, ξ is the velocity vector, λ is the relaxation time, f^{eq} is the equilibrium distribution function, and $-\frac{1}{\lambda}(f - f^{\mathrm{eq}})$ is the BGK collision operator of Bhatnagar et al. (1954). Equation (2) is discretized in the velocity space, the displacement space, and time, resulting in the discretized lattice BGK equation:

$$f_\alpha(\vec{x}_i + \vec{e}_\alpha \delta t, t + \delta t) = f_\alpha(\vec{x}_i, t) - \frac{1}{\tau}\left[f_\alpha(\vec{x}_i, t) - f_\alpha^{\mathrm{eq}}(\vec{x}_i, t)\right], \tag{3}$$

where $\vec{e}_\alpha$ is the velocity vector belonging to some discrete set depending on the lattice chosen, f_α is the distribution function associated with the corresponding lattice site velocity, $\vec{x}_i$ represents the location in physical space, δt is the time step, $\vec{e}_\alpha \delta t$ is the displacement step, and $\tau = \frac{\lambda}{\delta t}$ is the dimensionless relaxation time.

To simplify the computations, (3) is commonly separated into a local collision and a global propagation step, yielding the following numerical scheme:

$$\begin{aligned} \text{Collision:} \quad & \tilde{f}_\alpha(\vec{x}_i, t) = f_\alpha(\vec{x}_i, t) - \frac{1}{\tau}\left[f_\alpha(\vec{x}_i, t) - f_\alpha^{\mathrm{eq}}(\vec{x}_i, t)\right], \\ \text{Propagation:} \quad & f_\alpha(\vec{x}_i + \delta t \vec{e}_\alpha, t + \delta t) = \tilde{f}_\alpha(\vec{x}_i, t). \end{aligned} \tag{4}$$

The exact form of the velocity vector $\vec{e}_\alpha$ in (4) depends on the lattice configuration. In this study, we use the two-dimensional (2D), 9-velocity D2Q9 lattice model (Fig. 1) and the 3D D3Q19 lattice model, with 9 and 19 velocity vectors at each lattice site, respectively. The magnitude of the velocity vectors is derived from the assumption that all particles move with a constant speed, where the lattice speed or lattice constant is defined as: $c = \delta x/\delta t$. It can be shown that the lattice speed is related to the lattice speed of sound by $c_s = c/\sqrt{3}$. The corresponding equations and lattice configurations for other 2D and 3D lattice models are given, for example, in He and Lou (1997b).

For low Mach number flow conditions, the equilibrium distribution function f^{eq} in (4) can be derived by a Taylor series expansion of the Maxwell-Boltzmann equilibrium distribution, as shown by He and Lou (1997a):

$$f_\alpha^{\mathrm{eq}} = w_\alpha \rho \left[1 + 3(\vec{e}_\alpha \cdot \vec{u}) + \frac{9}{2}(\vec{e}_\alpha \cdot \vec{u})^2 - \frac{3}{2}\vec{u}^2\right], \tag{5}$$

where the vector $\vec{u}$ represents the macroscopic velocity, ρ is the macroscopic pressure, and w_α are lattice

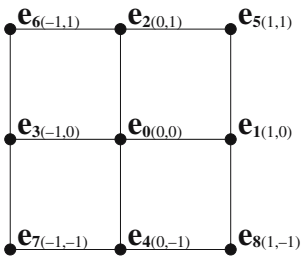

Fig. 1 Discretization of velocity space for the D2Q9 lattice

weights that depend on the lattice geometry. For the D2Q9 lattice model these weights are:

$$w_\alpha = \begin{cases} 4/9, & \text{for } \alpha = 0, \\ 1/9, & \text{for } \alpha = 1, 2, 3, 4, \\ 1/36, & \text{for } \alpha = 5, 6, 7, 8. \end{cases}$$

The macroscopic parameters, such as density, velocity, pressure, and viscosity, can be evaluated by taking statistical moments of the distribution function, leading to the following equations:

$$\begin{aligned} \rho(\vec{x}, t) &= \sum_{\alpha=0}^{8} f_\alpha(\vec{x}, t), \\ \rho\vec{u}(\vec{x}, t) &= \sum_{\alpha=0}^{8} \vec{e}_\alpha f_\alpha(\vec{x}, t), \\ p(\vec{x}, t) &= c_s^2 \rho(\vec{x}, t), \\ \nu &= (\tau - 1/2) c_s^2 \delta t, \end{aligned} \tag{6}$$

where $p = c_s^2 \rho$ is the isothermal ideal gas equation of state for the LBM. Thus, pressure and density in the LBM differ only by a constant factor, leading to only two macroscopic unknowns (density and velocity) in the lattice Boltzmann equations compared to three macroscopic unknowns in the NS equations (density, pressure, and velocity). Under the low Mach number assumption, using the Chapman-Enskog expansion (see Chapman and Cowling 1952), it may be shown that the macroscopic quantities obtained in this manner approximate solutions to the NS equations within $O((Ma)^2)$ (see, for example, Wolf-Gladrow 2000). We emphasize, however, that the LBM is not just another numerical method to solve the NS system; rather, it is a numerical method for solving the lattice BGK equation, which, under certain flow conditions, produces a very good approximation to NS flows.

2.2 Boundary conditions

The treatment of boundary conditions in the LBM deserves special attention as it differs from the one of traditional methods discretizing the NS equations. A variety of LBM schemes for open and closed boundaries exist, many of which have been reviewed by Yu et al. (2005). For the present work, a special emphasis was placed on choosing simple boundary conditions to benchmark the optimal designs that we obtain against those available in the literature.

Following Ladd (1994) and Behrend (1994) for closed boundaries, the no-slip bounce-back boundary condition was used, which replaces the collision step with a simple reversal of the distribution function f_α across the lattice symmetries; for example, for the D2Q9 lattice we have:

$$(f_1 \leftrightarrow f_3,\ f_2 \leftrightarrow f_4,\ f_5 \leftrightarrow f_7, \text{ and } f_6 \leftrightarrow f_8). \tag{7}$$

This effectively creates a no-slip boundary halfway between the boundary node and the node closest to the fluid.

For the inlet boundary condition, an equilibrium distribution velocity inlet condition was used, where the inlet velocity is prescribed and the density is determined from the propagated values inside the computational domain. Again, the propagation step remains untouched and the collision step is replaced by

$$\text{Collision: } \tilde{f}_\alpha(\vec{x}_i, t) = f_\alpha^{\text{eq}}, \tag{8}$$

where f_α^{eq} is a function of the inlet velocity as can be seen from (5).

For the outlet boundary condition a simple non-equilibrium density boundary condition was used. This boundary condition is the LBM equivalent to pressure boundary conditions used in NS-based flow solvers due to the fact that pressure and density differ by a constant factor in the LBM as discussed in Section 2.1. For the density boundary condition the collision process is the same as for the internal nodes, except that the density used to calculate the equilibrium distribution function f_α^{eq} is prescribed and not calculated from the propagated values.

Finally, it should be noted that due to the direct relation between density and pressure shown in (6), the LBM requires only two boundary conditions in comparison to the three boundary conditions needed in NS-based methods.

2.3 Lattice Boltzmann method based topology optimization

For topology optimization purposes, the above LBM scheme is augmented by a continuous optimization model, smoothly "transforming" fluid sites into solid and vice versa. We adopt the LBM porosity model introduced by Spaid and Phelan (1997) for solving the Brinkman equations for porous flows in place of the NS equations. The porosity model requires only a minor modification of the collision step (4) in the LBM algorithm. Instead of using the macroscopic velocity (6) when evaluating the equilibrium distribution (5), we scale it by a factor $0 \leq (1 - \beta(\vec{x})\tau) \leq 1$, where the parameter β is related to the porosity, defined in detail by Spaid and Phelan (1997). The parameters $d(\vec{x}) = \beta(\vec{x})\tau$ at every lattice point are then used as the design

variables. The macroscopic velocity $\tilde{\vec{u}}$ in a porous region can be computed as follows:

$$\tilde{\vec{u}}(t, \vec{x}) = (1 - d(\vec{x}))\, \vec{u}(t, \vec{x}), \tag{9}$$

where $\tilde{\vec{u}}(t, \vec{x})$ is substituted into (5). When $d(\vec{x}) = 0$, $\vec{x}$ is a pure fluid point, when $d(\vec{x}) = 1$, $\vec{x}$ is a pure solid point, and when $0 < d(\vec{x}) < 1$, $\vec{x}$ is occupied by a porous medium. In our computational experience we obtained better convergence results when, instead of the linear scaling in (9), we used the following polynomial scaling:

$$\tilde{\vec{u}}(t, \vec{x}) = (1 - d(\vec{x})^{\kappa})\, \vec{u}(t, \vec{x}), \tag{10}$$

for $\kappa > 1$. We obtained best results with $\kappa \in [2, 3]$.

This simple idea allows the control of the fluid in a simple and continuous fashion. By using the LBM we can thus solve the same physical system as done by Borrvall and Petersson (2003), applying a conventional NS-based fluid solver for the solution of the Brinkman equation. However, whereas in the approach proposed by Borrvall and Petersson one must drive the inverse permeability to infinity to recover pure solid, thus leading to numerical problems, we can continuously vary between solid and fluid by letting $0 < d(\vec{x}) < 1$. A brief discussion of the NS-based optimization problem in Section 2.5 will further illustrate these differences.

With respect to the use of the LBM in this study, we consider only optimization problems for steady-state flow conditions. To write the governing equations in a compact form, all design variables $\{d(\vec{x}_1), \ldots, d(\vec{x}_L))\}$ are collected into a vector $\vec{d} \in [0, 1]^L$, where $L \in \mathbb{N}$ is the number of lattice points. Similarly, all distribution functions $f_\alpha(\cdot)$ are collected into a vector $\vec{f} \in \mathbb{R}^{rL}$, where r is the number of distribution functions at each lattice point. The steady-state variant of the time-dependent LBM (4) is formulated as follows:

$$\Pi(\vec{f}) - \vec{f} + \vec{\Delta}(\vec{d}, \vec{f}) = \vec{0}. \tag{11}$$

The mapping of $\Pi : \mathbb{R}^{rL} \to \mathbb{R}^{rL}$ is responsible for the "propagation" part of the discrete Boltzmann equation. The collision operator $\vec{\Delta}$ is the only design-dependent part of the system and is highly nonlinear in $\vec{f}$.

A generic topology optimization problem for steady-state flow conditions can now be written as follows:

$$\min_{(\vec{d}, \vec{f}) \in [0,1]^L \times \mathbb{R}^{rL}} \mathcal{F}(\vec{d}, \vec{f}),$$

$$\text{s.t.} \begin{cases} \vec{1}^T \vec{d} \geq \gamma L, \\ \vec{f} \text{ solves (11)}, \end{cases} \tag{12}$$

where $\mathcal{F}$ is a particular performance functional. Note that the above optimization problem has a control in coefficients structure. Assuming that the performance functional and the governing steady-state equations are smooth functions of the optimization variables, the problem (12) can be solved by any large-scale gradient-based optimization algorithm. In this study, we use SNOPT by Gill et al. (2002), a commercial implementation of a penalty-based sequential quadratic programming algorithm, for mid-size problems and the method of moving asymptotes (MMA) by Svanberg (1987), a sequential convex approximation-based algorithm, for problems where the memory requirements of SNOPT exceed our hardware constraints.

2.4 Objective and constraint functions

In this study, two different objective functions were used: drag and pressure drop. The drag in a lattice Boltzmann model can be determined via a variety of methods (see, for example, Mei et al. 2002). However, the summation of all momentum sinks due to the porosity effect can be most readily applied to topology optimization problems due to the use of the porosity model for the entire flow domain. For this method, the drag is determined by the following summation over all lattice points in the flow domain:

$$D = \sum_L ((\rho u)_{\text{pre}} - (\rho u)_{\text{post}}), \tag{13}$$

where u is the velocity in the free-stream direction, and "pre" and "post" represent the fluid before and after the collision process during which the porosity momentum sink is applied.

The second objective function used is the pressure drop across the system approximating the total pressure drop and thus total mechanical energy loss in the system. The appropriateness of this approximation is briefly discussed in the following. Assuming uniform inlet and outlet flows, the total pressure drop can be expressed as

$$\Delta p_T = \left(p + \frac{1}{2}\rho V^2 + \gamma z\right)_{\text{in}} - \left(p + \frac{1}{2}\rho V^2 + \gamma z\right)_{\text{out}},$$

where γ is the specific weight, $\gamma = \rho g$, and g is the gravity. Assuming that the elevation change is negligible, the equation reduces to:

$$\Delta p_T = \left(p + \frac{1}{2}\rho V^2\right)_{\text{in}} - \left(p + \frac{1}{2}\rho V^2\right)_{\text{out}}.$$

If we now consider the small Mach number restriction of the LBM, the velocity terms become negligible in the above equation, leading to:

$$\Delta p_T = p_{\text{in}} - p_{\text{out}}.$$

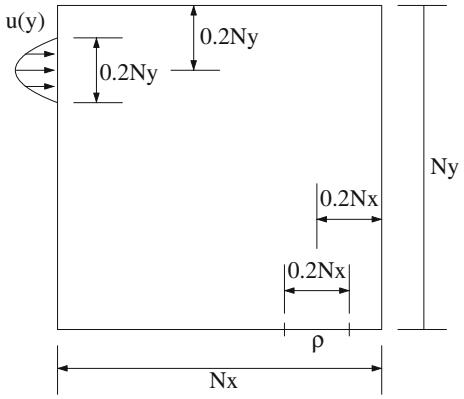

Fig. 2 Pipe bend design domain with inlet and outlet conditions

In general, the inlet and outlet flows are not uniform. Therefore, we formulate the objective functions as the difference between the sum of all inlet densities and the sum of all outlet densities, leading to the following objective function for the pressure drop:

$$p_{\text{drop}} = \sum_{\text{inlet}} p_{\text{in}} - \sum_{\text{outlet}} p_{\text{out}}. \tag{14}$$

The only optimization constraint used in this study is a volume constraint. We prescribe that at most a given fraction of the control volume is allowed to be occupied by a fluid, and the remainder must be solid.

2.5 Navier-Stokes equations-based topology optimization

In comparison to the lattice Boltzmann-based model discussed in Section 2.3, the original idea of Borrvall and Petersson (2003), which was formulated for Stokes flows, but was later extended to NS fluids, can be explained as follows. Instead of the initial system of partial differential equations (PDEs), the incompressible NS equations in this case,

$$\frac{\partial \vec{u}}{\partial t} + (\vec{u}\nabla)\vec{u} = -\frac{1}{\rho}\nabla p + \nu\Delta\vec{u}, \tag{15}$$

one considers a modified system augmented with an additional term, which will eventually depend on the

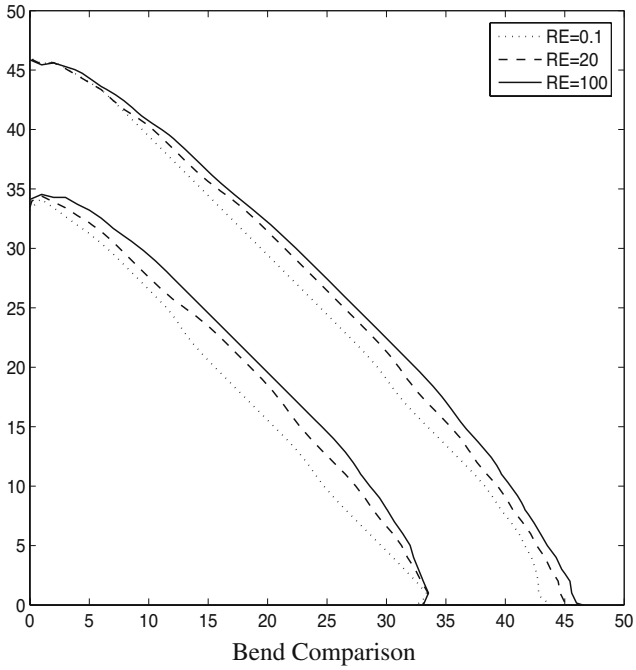

Fig. 4 Comparison between pipe bends at Re=0.1, 20, and 100

design variable. The latter system may be identified as a system of (nonlinear) Brinkman or Darcy-Stokes equations, and it describes a flow of viscous fluid through a porous medium (see, for example, Brinkmann 1947; Allaire 1990):

$$\left.\begin{aligned} -\nu\vec{\Delta}\vec{u} + \vec{u}\cdot\vec{\nabla}\vec{u} + \alpha(d)\vec{u} + \vec{\nabla}p &= \vec{F}, \\ \operatorname{div}\vec{u} &= 0 \end{aligned}\right\}, \quad \text{in } \Omega. \tag{16}$$

In system (16), $\vec{u}$ is the flow velocity, p is the pressure, ν is the kinematic viscosity, $\vec{F}$ are the forces acting in the domain, and α is the inverse permeability of the porous medium as a function of the design variable d. Ω is the 2D or 3D domain on which the Brinkman system (16) is considered, and has a regular boundary Γ. In addition, appropriate boundary conditions must be prescribed.

Now by spatially varying the inverse permeability/porosity α of the porous medium, we may control the behavior of the fluid. Driving the porosity (α^{-1}) to infin-

Fig. 3 Pipe bend optimization results at various Reynolds numbers

Table 1 Comparison of pipe bend optimizations at different Reynolds numbers

Re	Initial objective	Final objective
0.1	0.0061	0.0001538
1	0.0607	0.0015488
10	0.6109	0.0157750
20	1.2197	0.0333344
100	3.9299	0.1903172

The objective values are the merit function values returned by SNOPT.

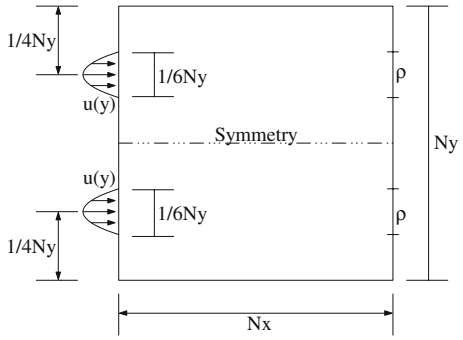

Fig. 6 Two pipes design domain with inlet, outlet, and symmetry conditions

ity, we hope to recover the starting NS equations; while setting it to zero we should hopefully stop the fluid, thus simulating a solid wall at a given point. Following Borrvall and Petersson (2003), Evgrafov (2005a), and Evgrafov (2005b), this can, for example, be achieved if the permeability α^{-1} is related to the design variable d using a convex, decreasing, and nonnegative function $\alpha : [0, 1] \to \mathbb{R}_+ \cup \{+\infty\}$, defined as $\alpha(d) = d^{-1} - 1$. Thus $d(\vec{x}) = 0$ corresponds to zero permeability at $\vec{x}$ (i.e., a solid), while $d(\vec{x}) = 1$ corresponds to infinite permeability (i.e., 100% fluid).

If the design variable d is now assumed to reside in the control set $\mathcal{H}$ as follows,

$$\mathcal{H} = \left\{ d \in L^\infty(\Omega) \mid 0 \le d \le 1, \text{ a.e. in } \Omega, \int_\Omega d \le \gamma |\Omega| \right\},$$

where $0 < \gamma < 1$ is the maximal volume fraction that can be occupied by the fluid, we can obtain the following optimization problem:

$$\min_{(\vec{d},\vec{u})} \mathcal{F}(\vec{d}, \vec{u}),$$
$$\text{s.t.} \begin{cases} \vec{d} \in \mathcal{H}, \\ \vec{u} \text{ weakly solves (16)}, \end{cases} \tag{17}$$

where $\mathcal{F}$ is a particular performance functional (objective function). It should be stated that system (17) does not necessarily possess a unique solution for an optimal design $\vec{d}$. For further details, the interested reader is referred to Evgrafov (2005a,b).

We emphasize that driving the permeability to zero at a given point (a solid), the inverse permeability α must be driven to a very large value, ideally infinity. This leads to computational challenges when finite element methods or finite volume methods are used to numerically solve the underlying system of PDEs. As discussed in Section 2.3, this problem can be avoided by the LBM porosity model previously introduced.

3 Numerical implementation

In this section we briefly summarize the key components of the numerical implementation of the proposed optimization method. This includes finding the steady-state solution, determining the sensitivities and parallelization issues.

The standard LBM algorithm is an explicit time-marching scheme for computing time-dependent flows. To compute steady-state flow solutions, the flow needs to be advanced in time until convergence, that is, the difference between two or more successive flow states vanishes. The steady-state condition can be written as follows:

$$|\vec{f}_t - \vec{f}_{t-1}|_\infty \le \varepsilon \tag{18}$$

for a small $\varepsilon > 0$. Satisfying the above condition is equivalent to finding an approximate solution to the

Fig. 5 Bend design vs optimizer iteration (Re=1)

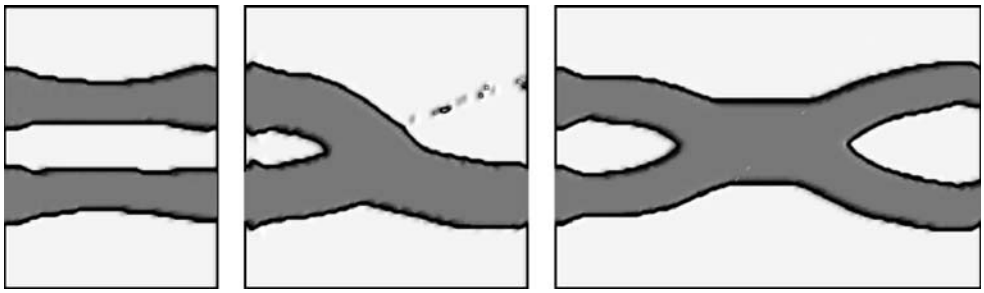

Fig. 7 Illustration of the density outlet condition for two pipes at Re = 1.66 with respect to the inlet diameter. The design domain differs slightly from Fig. 6

fixed-point problem (11), which can be written in compact form as follows:

$$\vec{R}(d,\,\vec{f}) = \vec{M}(d,\,\vec{f}) - \vec{f} = \vec{0}, \tag{19}$$

where $\vec{R}$ denotes the residual vector. Here, the operator $\vec{M}$ performs one collision and one propagation step, which is exactly what is needed to advance the flow to the next time step.

The sensitivities of the performance functional $\mathcal{F}$ in (12) are computed analytically by the adjoint method. The gradient of the objective function $\mathcal{F}$, with respect to the design variables d_i, can be written as follows:

$$\frac{d\mathcal{F}}{dd_i} = \frac{\partial \mathcal{F}}{\partial d_i} + \frac{\partial \mathcal{F}^t}{\partial \vec{f}}\,\frac{d\,\vec{f}}{dd_i}, \tag{20}$$

where $\vec{f}$ is the distribution function governed by the fixed-point formulation (19). Due to the large number of design variables, the gradients of $\mathcal{F}$ are computed by the adjoint method as follows:

$$\vec{J}^t\,\vec{a} = \frac{\partial \mathcal{F}}{\partial\,\vec{f}} \tag{21}$$

$$\frac{d\mathcal{F}}{dd_i} = \frac{\partial \mathcal{F}}{\partial d_i} - \vec{a}^t\,\frac{\partial\,\vec{R}}{\partial d_i}, \tag{22}$$

where $\vec{J}^t$ is the transpose of the Jacobian of the fixed-point problem (19). For a $nx \times ny$ D2Q9 lattice, the Jacobian $\vec{J}$ is a sparse unsymmetric square matrix of size $(nx \cdot ny \cdot 9)^2$. In the presence of no-slip boundary conditions the Jacobian $\vec{J}$ is singular, which, in general, precludes the use of the Implicit Function Theorem to perform the sensitivity analysis. This problem can be easily dealt with by excluding some of the "superfluous" particle distributions associated with the no-slip boundary conditions from the fixed-point system (19).

In this study, we compute the steady-state flow with the standard LBM, explicit time marching algorithm. Although one can expect that a large number of time steps is needed to reach steady-state, this approach features improved numerical stability and robustness over implicit schemes. In addition, it is well suited for parallelization using a domain decomposition strategy. Because the collision step occurs locally at each lattice site and the propagation step only impacts neighboring lattice sites, only information along the boundary of the subdomain treated by each processor must be transferred to the corresponding neighboring processor. Thus, the computational time scales almost linearly for parallel computations, making the LBM ideal for parallelization.

The computation of the design sensitivities requires solving the linear system (21). For practical reasons, we apply a parallel direct sparse solver to this problem, namely the parallel version of the SuperLU solver (see Li and Demmel 2003), acknowledging that greater parallel scalability could be obtained with iterative solvers.

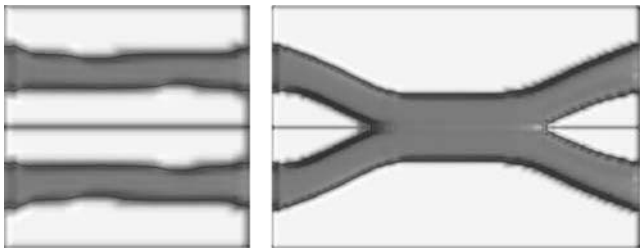

Fig. 8 Example of a short and long double-pipe

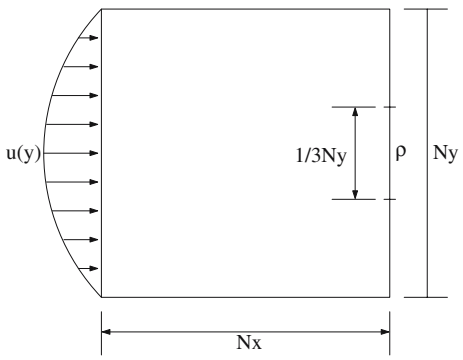

Fig. 9 Diffuser design domain with inlet and outlet conditions (cross section for 3D)

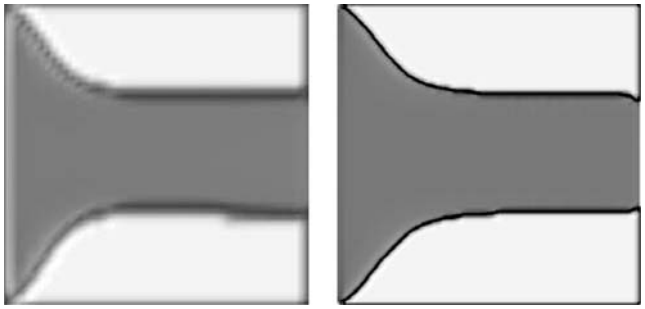

50 by 50 Lattice (SNOPT) | 100 by 100 Lattice (MMA)

Fig. 10 Diffusers at Re = 100

4 Numerical examples

To demonstrate the viability of the LBM for topology optimization, we consider numerical examples analogous to those presented by Borrvall and Petersson (2003). In addition, a simple 3D topology optimization of a diffuser will be presented.

In our two-dimensional (2D) computations we use $(nx-1)\times(ny-1)$ design variables for a lattice of size $nx \times ny$, i.e., one design variable between four lattice sites. In the 3D case, we place one design variable between eight lattice points. We obtain the porosity at each node, required by (9), through interpolating from the four/eight surrounding design variables, which results in a small filtering/averaging effect that leads to a smoothing of the results. This smoothing yields density gradients at the fluid–solid interface. Therefore, the resulting plots of nodal densities presented below seem a bit "blurred" at the interfaces.

4.1 Pipe bend (2D)

The first numerical example presented is that of a pipe bend (see Fig. 2), analogous to Borrvall and Petersson (2003). We minimize the pressure drop between inlet and outlet, which has a comparable effect to the power loss objective used by Borrvall and Petersson. The volume fraction of fluid is restricted to at most 25%, which is again equivalent to the value used by Borrvall and Petersson. As shown in Fig. 2, a parabolic velocity profile at the inlet and the density at the outlet are prescribed.

Using the described setup of the pipe bend design problem and performing the optimization at various Reynolds numbers (Re=0.1, 1, 10, 20, and 100), where Re is defined with respect to the inlet width (L=0.2Ny), we obtain the results shown in Fig. 3. From these results, it can be seen that the geometry of the pipe is almost straight for low Reynolds numbers and gradually increases curvature for larger Reynolds numbers, as would be expected from the physics of the problem. In Fig. 4 we plot the wall boundaries for three Reynolds numbers (Re=0.1, 20, and 100). Here the wall boundaries for Re=1 and 10 were omitted because they almost coincide with the boundary for Re=0.1. The observed increase of the curvature for larger Reynolds numbers is due to the following competing physical effects, which lead to the optimal solution. First, to reduce the shear stress along the walls (τ_w), the pipe must be as short and as wide as possible. This explains the resulting straight pipe shown by Borrvall and Petersson (2003), who use a Stokes model where the power dissipation depends solely on the shear. Second, to reduce the momentum loss in the pipe due to the turning of the flow, it is advantageous to turn the flow slowly and continuously, rather than abruptly. Thus, the optimal solution will result from the combined effect of minimizing the shear stresses at the walls and minimizing the momentum loss due to the turning of the flow. Therefore we expect a nearly straight pipe for low Reynolds numbers (Stokes limit) and increasing curvature of the pipe for larger Reynolds numbers, as shown by the numerical results in Fig. 3.

Table 1 displays the initial and final objective values for the five different Reynolds numbers used, where the objective values are given in lattice units. It should be noted that the presented objective values are the merit function values returned by SNOPT, which are equivalent to the objective as the optimization converges. It was found that it is advantageous to start the optimization with an infeasible solution ($d = 0.1$ everywhere), resulting in larger merit function values, because the convergence to steady state in the LBM program slows

Table 2 Results from the optimization of a diffuser on a 50×50 lattice

Re	Initial objective	Final objective	Opt. iterations	Avg. LBM iterations
100	30.563323	30.372510	1115	20091

The objective values are the merit function values returned by SNOPT.

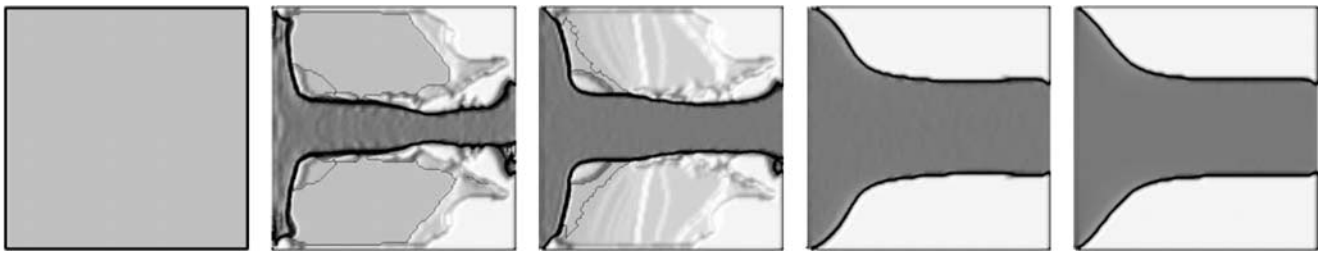

Fig. 11 Optimization steps for a diffuser at Re = 100 on a 100 × 100 lattice using the MMA

down significantly for larger porosities due to the larger pressure drop that must be established.

Figure 5 shows the layout of the pipe bend at different optimizer iterations. The reader can see from the figure that the general topology is obtained after only a few iterations, however, convergence to an accuracy of $\epsilon = 10^{-8}$, which is the maximum achievable accuracy given the current flow solutions, requires significantly more iterations. Thus, based on the number of optimizer iterations, which is 2,840 for the presented problem, and the average number of LBM iterations, which is approximately 20,000 for the given problem size, it can be seen that the optimization process is fairly costly. This is a concern because both iteration numbers, in particular the one for the LBM steady-state iterations, increase with increasing lattice sizes. Because the general topology is achieved early in the optimization process, the optimizer convergence could be improved, for example, by switching to a shape optimization approach once the general topology has been found. At the costs of decreased robustness and reduced parallel scalability, the convergence of the LBM time-marching scheme towards steady-state flow solutions can also be significantly improved by switching to implicit schemes, as suggested by Bernaschi and Succi (2003).

4.2 Two pipes (2D)

The next numerical example is that of two inlet and two outlet ports (Fig. 6), where the fluid volume is restricted to at most 33% of the design domain. It will be shown that if the ports are sufficiently far apart, then the connecting pipes merge to minimize the pressure drop.

For this problem the modeling of the LBM boundary conditions plays an important role. Using a traditional NS-based fluid solver, one would prescribe the velocity at both the inlet and the outlet as was done by Borrvall and Petersson (2003). This ensures that an exit flow occurs at both outlets. However, using the LBM, one cannot impose these boundary conditions, and the exit boundary must be a density outlet condition. Using the density outlet conditions, the flow can find an optimal solution that brings all of the flow to one exit (Fig. 7), which is insightful from a topology optimization point, but is not desired for the current problem.

An alternative option is to prescribe the velocity at one of the exits and the density at the other exit. However, this condition forces the two pipes to join and thus does not lead to the desired results. Thus, given the LBM boundary conditions, this problem can only be solved analogous to the NS solution, if a constraint

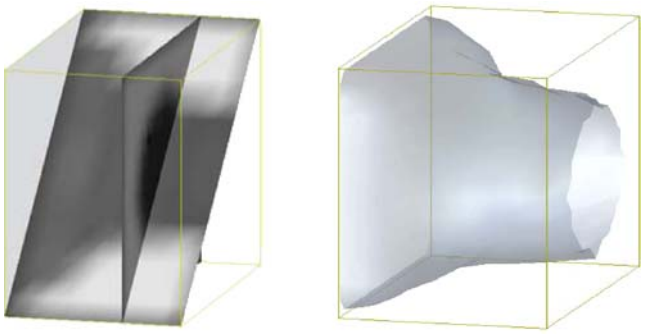

Fig. 12 3D diffuser optimization (Re=50)

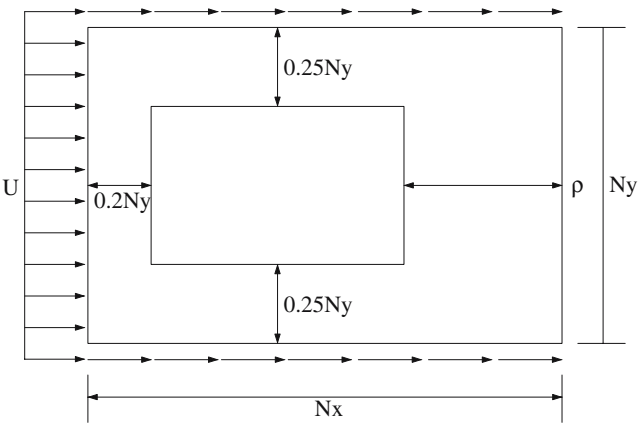

Fig. 13 External flow design domain with corresponding boundary conditions

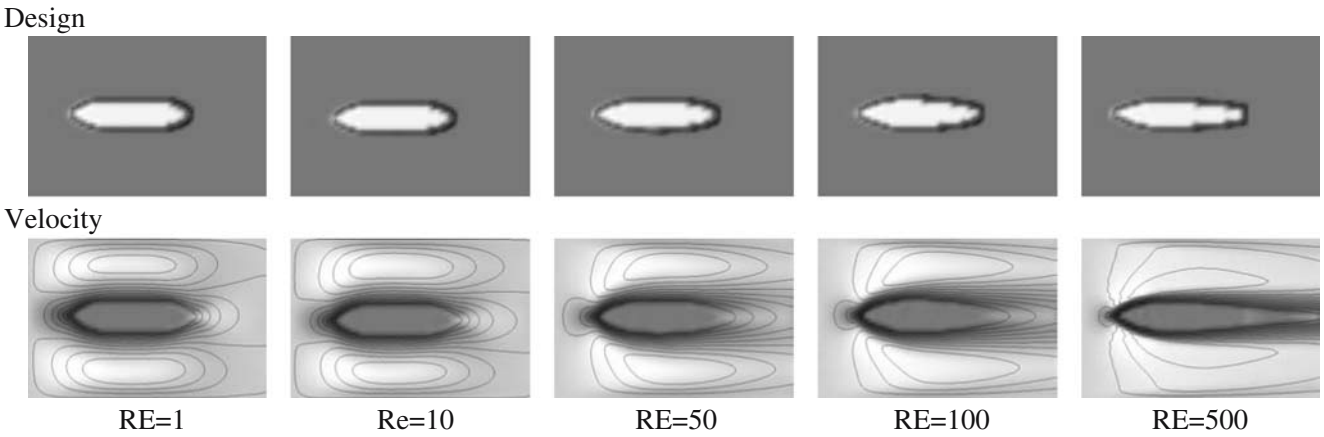

Fig. 14 Optimal design solutions and corresponding velocity profiles with isolines for an object in external flow at different Reynolds numbers on a 75 × 50 lattice

is added that forces the flow rate to be equivalent at both outlets, or if symmetry boundary conditions are used between the top and bottom portion of the design domain. For the presented data, the symmetry boundary conditions were used due to their ease of implementation and reduced computational effort. However, the symmetry boundary condition restricts the topology optimization to symmetric solutions. Results for this computation can be seen in Fig. 8 for both a short and a long domain.

4.3 Diffuser (2D/3D)

The next example is that of a diffuser minimizing the pressure drop over the system while the volume fraction of fluid is restricted to at most 25%, which is equivalent to the value used by Borrvall and Petersson (2003). As shown in Fig. 9, a parabolic velocity inlet boundary condition and a density outlet boundary condition are used. This problem has been studied by Cabuk and Modi (1992), leading to similar results; however, due to the use of differing boundary conditions, a detailed comparison of the results cannot be made.

The optimized design of the diffuser at a Reynolds number of 100 is compared for two different lattice sizes, 50 × 50 and 100 × 100 in Fig. 10. From Fig. 10 one can see that the results are similar to those obtained by Borrvall and Petersson (2003). The initial objective value (pressure drop), final objective value, number of optimizer iterations, and average number of LBM iterations to steady state per optimization are presented in Table 2 for the nozzle on the 50 x 50 lattice (the objective values are given in lattice units). Snapshots of the optimization process for the diffuser on the 100 × 100 lattice are shown in Fig. 11. From these one can see that the optimization process does not occur symmetrically. However, the final result for the 100 × 100 lattice is a symmetric diffuser. In addition, one sees that the topology is clearly visible after 50 iterations and that the remaining iterations are used to determine the exact shape of the nozzle. This trend was already observed for the bend in Section 4.1.

Having shown the viability of the LBM-based topology optimization approach for the 2D diffuser problem, we illustrate the applicability of the method to the 3D formulation of the same design problem, as shown in Fig. 12. For practical purposes we use a coarse 10×16×16 lattice at a Reynolds number of 50,

Table 3 Comparison of optimization results for different Reynolds numbers on a 75 × 50 lattice

Re	Initial objective	Final objective	Opt. iterations	Design circumference	Design height
1	0.000622574	0.000064718	391	76.90	8.098
10	0.006333201	0.000660479	578	77.58	8.092
50	0.039016299	0.004019155	88	77.84	8.092
100	0.10103713	0.009828596	736	79.14	9.049
500	0.1147103	0.099731694	246	84.33	8.064

The objective values are the merit function values returned by SNOPT

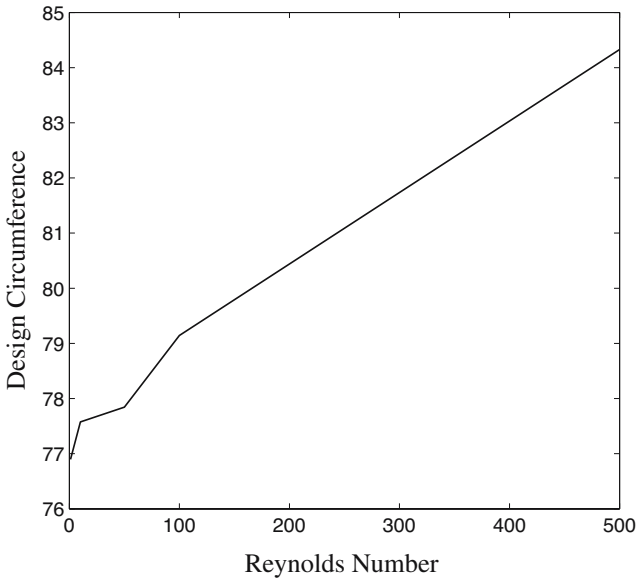

Fig. 15 Design circumference vs Reynolds number on a 75 × 50 lattice

minimize the pressure drop between inlet and outlet, and restrict the volume fraction of fluid to at most 50%. As shown by the velocity contour plot in Fig. 12, the 3D application of the lattice Boltzmann-based topology optimization leads to a result similar to the one achieved for the 2D case.

4.4 External flow (2D)

The final example is the optimization of the topology of an object in an external flow (Fig. 13) such that the drag caused by the object is minimized, leading to a rugby ball shape at low Reynolds numbers and a symmetric airfoil for larger Reynolds numbers. A similar minimum-drag problem was treated analytically by Pironneau (1973, 1974), where the optimal shape of the front and back angles of a rugby ball-shaped object were investigated in Stokes flow, leading to a front and back angle of 90° at the optimum. It will be shown that comparable results are obtained with topology optimization.

For the current problem the boundary conditions at the inlet, top, and bottom were set to a constant velocity in the x-direction and zero velocity in the y-direction. The outlet boundary condition is the density condition. For these problems the fluid volume was restricted to at most 93.3%, which is equivalent to the 90% used by Borrvall and Petersson (2003), given that our design domain is rectangular. Because the outlet velocity cannot be prescribed, more space must be allowed behind the airfoil to allow the flow to develop. It should be noted here that for exact solutions, the upstream, downstream, top, and bottom boundaries should be separated much further away from the object.

4.4.1 Optimal designs on a small lattice

Figure 14 shows how the optimized shape and corresponding velocity profile vary for different Reynolds numbers. Table 3 shows the corresponding initial drag, optimized drag, convergence data, design circumference, and design height. It should be noted at this point that to obtain the solution at Re=500, a restart from an intermediate solution at Re=100 was needed to avoid divergence problems due to large Mach numbers in the lattice Boltzmann algorithm. Here the critical length used for the Reynolds numbers is the length of the design domain. From the results it can be seen that the optimization process leads to rugby ball-like shapes at all Reynolds numbers. However, the designs at low Reynolds numbers are more blunt and short, whereas the designs at larger Reynolds numbers take a more streamlined and elongated form, similar to that of an airfoil.

These results are expected due to the competing effects of form/pressure drag and friction drag, which combine to the total drag, the objective function for the current problems. As implied by the definition of the Reynolds number (inertia force/viscous force), one can

Fig. 16 Optimal design solutions for an object in external flow at different Reynolds numbers on a 225 × 150 lattice

Table 4 Comparison of optimization results for different Reynolds numbers on a 225 × 150 lattice

Re	Initial objective	Final objective	Opt. iterations	Design circumference	Design height
1	0.00018045865	0.000019369667	288	227.42	26.96
10	0.0018404837	0.00019789287	180	233.02	26.05
100	0.029503281	0.0029714002	306	249.27	23.89

The objective values are the merit function values returned by SNOPT.

see that viscous forces (friction drag) dominate at low Reynolds numbers, whereas inertia forces (pressure drag) dominate as the Reynolds number is increased. Because friction drag is generally related to the exposed surface area of an object and pressure drag is related to how streamlined an object is (often tied to the cross-sectional area of a body that is facing in the direction of the flow), one would expect the following design features at the different Reynolds numbers. For low Reynolds number flows, we expect a minimum drag design that minimizes the friction drag by reducing the surface area of the object, leading to fairly blunt objects. At larger Reynolds numbers, we expect a minimum drag design that focuses on reducing the pressure drag by streamlining the object, leading to an increased surface area.

From Fig. 14 one can clearly see that the optimal design progresses from a blunt rugby ball-shaped object toward a streamlined airfoil-like object as the Reynolds number is increased. In addition, Table 3 and Fig. 15 show that the circumference of the optimal designs increases with increasing Reynolds number as predicted above. However, it can also be seen from Table 3 that while the optimal designs become increasingly streamlined at larger Reynolds numbers, their cross section (height) facing the direction of the flow remains constant or increases with increasing Reynolds numbers for the designs on a 75 × 50 lattice. While a decreased cross section is not required for a streamlined design, it was expected for the current designs. A reason for this counterintuitive result could be the limited resolution possible on the small lattice, warranting a study of the optimal designs on a larger lattice.

4.4.2 Optimal designs on a large lattice

Increasing the lattice size yields better defined geometries. This is illustrated in Fig. 16, which shows the optimized material distributions at Re = 1, 10, and 100 on a 225 × 150 lattice. Table 4 shows the corresponding initial drag, optimized drag, convergence data, design circumference, and design height. The higher resolution of the material distribution leads to a much clearer defined airfoil in comparison to the design on the 75 × 50 lattice and it can be seen from the results in Table 4 that the height of the optimal designs decreases with increasing Reynolds number. The clearly defined geometries shown in Fig. 16 for the 225 × 150 lattice are well suited for comparison with the analytically determined minimum-drag designs by Pironneau (1973, 1974), who obtained front and back angles of 90° at the optimum. Figure 17 shows the outlines of the optimal designs with a superimposed 90° angle at the front and back of the designs. One can see that the designs obtained with topology optimization agree closely with the analytical shape optimization results obtained by Pironneau (1973, 1974). At Re = 1 the front and back

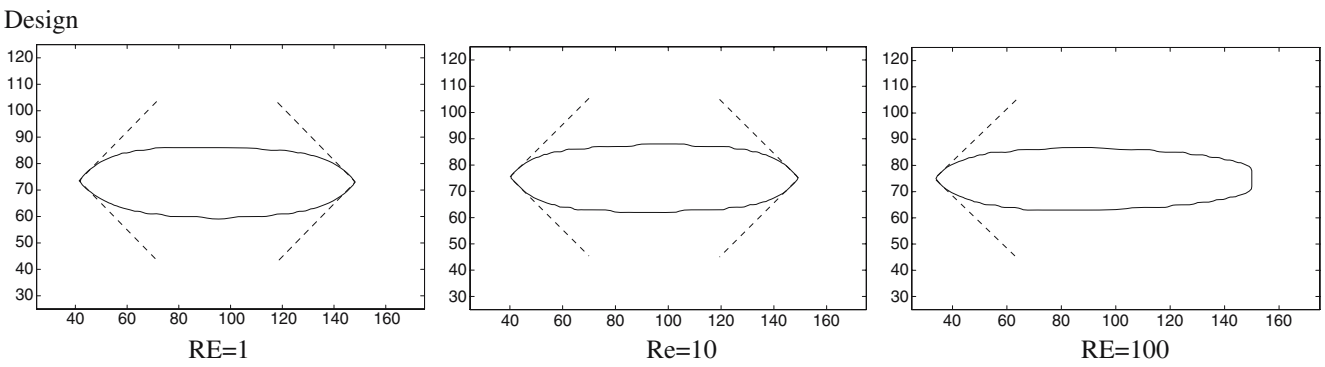

Fig. 17 Optimal design outlines with superimposed 90° angles at the front and back of the design for different Reynolds numbers on a 225 × 150 lattice

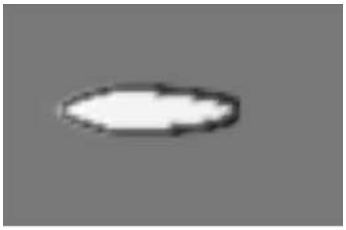

Lattice Size: 75 X 50

Lattice Size: 150 X 100

Lattice Size: 225 X 150

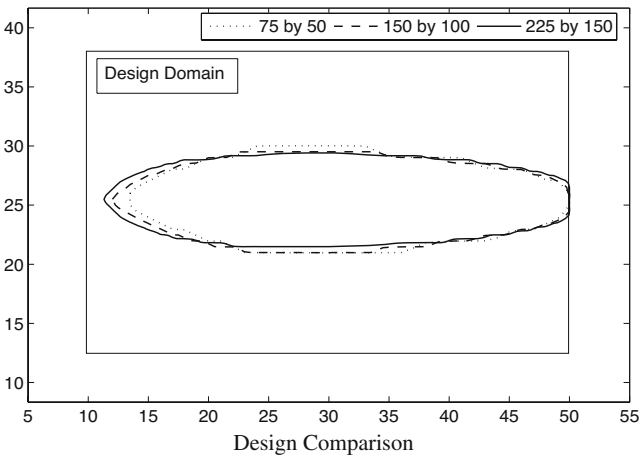

Fig. 18 Resolution increase at Re = 100

of the design closely match the Stokes flow solution, which predicts a 90° angle. With the exception of the back of the optimal solution at Re = 100, which is "cut off" by the limited design domain length, the larger

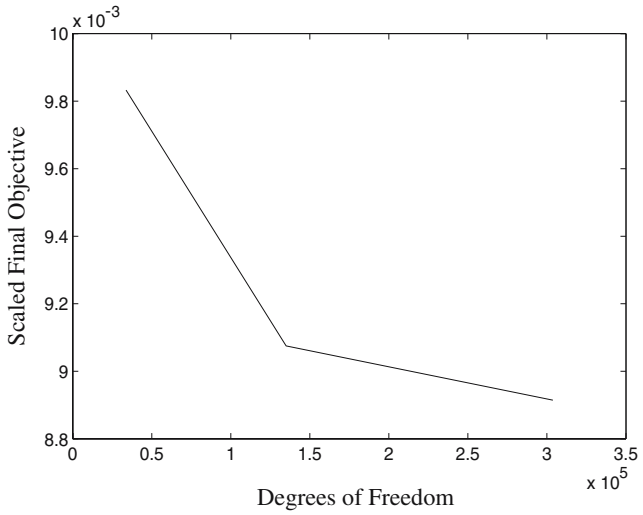

Fig. 19 Degrees of freedom vs scaled final objective at Re = 100

Reynolds number designs also seem to follow the 90° Stokes flow result. However, for the designs at larger Reynolds numbers, the angle narrows sooner than at Re = 1, leading to more streamlined results.

The differing results between the small and large lattice sizes warrant an analysis of the influence of the domain size on optimization results. To do so, we consider three scenarios. First, we simply scale up the complete problem, improving its resolution by increasing the lattice size and the size of the design domain. Second, we keep the size of the design domain and its relative position constant while increasing the lattice size, thereby testing the effect of the boundaries on the solution. Third, we keep the lattice size constant, but increase the design domain to investigate the effect of the design domain size on the optimal design.

4.4.3 Resolution increase

Figure 18 and Table 5 show the effect of increasing the lattice size on the optimized design solution for three lattices (75×50, 150×100, and 225×150) at Re = 100. Based on the results shown, we can reemphasize the observation made in Section 4.4.2 that the design geometries become clearer defined due to the improved resolution at the boundary. Furthermore, Fig. 19 shows

Table 5 Comparison of optimization results for different lattice sizes at Re = 100

Lattice size	Final objective	Optimizer iterations	Degrees of freedom
75×50	0.009828596	736	33,750
150×100	0.009075002	580	135,000
225×150	0.008914201	306	303,750

The objective values are the merit function values returned by SNOPT and were scaled to the result on the 75 by 50 lattice.

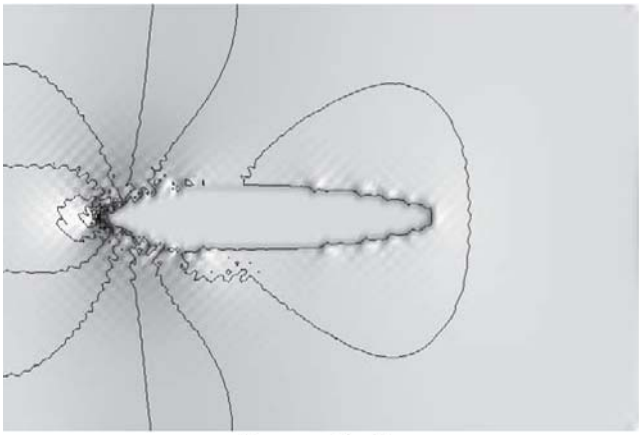

Fig. 20 Pressure isolines for a drag-minimized object in external flow at Re = 100 on a 150 × 100 lattice

a good convergence pattern of the objective function at the optimum as the number of degrees of freedom of the optimization problem is increased. For the largest lattice, more then 300,000 degrees of freedom are used, which is currently the maximum problem size solvable with the direct solver for the linear system in the sensitivity analysis on our computer system. Table 5 shows that the number of optimizer iterations also decreases for the larger design domain, most likely due to the smoother boundaries, which in turn lead to improved sensitivities and a faster convergence. Finally, Fig. 20 shows the pressure isolines for the 150 × 100 lattice. While the general pressure distribution around the airfoil is correct, the pressure contours in the boundary layer around the airfoil indicate that the lattice is still not fine enough to show smooth pressure isolines. However, despite the improved clarity of the optimal designs with increasing lattice size, the similarity between the designs on different lattices can be clearly seen in the last plot of Fig. 18. Thus, while an increased resolution produces more accurate and better defined optimal designs, the obtained shapes for the various design domain sizes are similar. Therefore, the choice of the size of the computational domain strongly depends on the user's objective. If one simply wants to generate concept ideas for designs, a smaller lattice size might be sufficient. However, if accurate results are needed for analysis purposes, a large domain size is preferable.

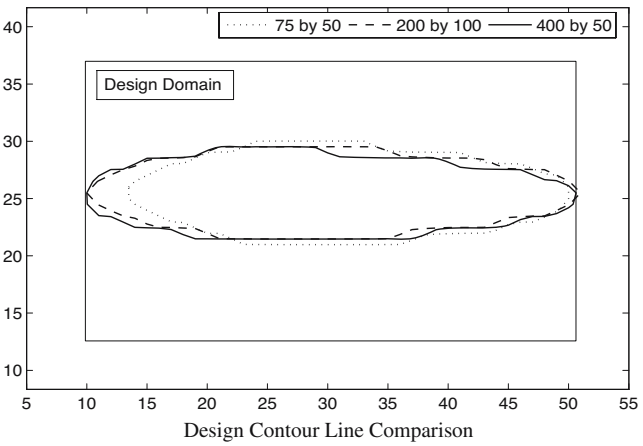

Fig. 21 Increased lattice size/constant design domain

Table 6 Comparison of optimization results for different lattice sizes with constant design domains at Re = 100

Lattice size	Final objective
75 × 50	0.0098326583
100 × 50	0.0094531925
200 × 50	0.0091260563
400 × 50	0.0091550179
200 × 100	0.0060621081

The objective values are the merit function values returned by SNOPT.

4.4.4 Increased lattice size/constant design domain

Figure 21 and Table 6 show the effect of using varying lattice sizes with a constant design domain of 40 × 25 lattice units located at a constant relative position with respect to the lattice size. From the results in Table 6 one can see that an increase of the lattice size leads to improved objective values due to the decreased effect of the boundaries on the optimal design. Here it should be pointed out that increasing the height of the domain has a significantly larger effect than a simple elongation of the domain, showing that the upper and lower boundaries have a stronger impact on the objective values than the inflow and outflow regions. However, despite the different objective value results, the final design topologies for the different lattice sizes were similar, as is shown in Fig. 21. Thus, an increased lattice size will produce a more accurate flow model, but not necessarily a significantly improved optimal design.

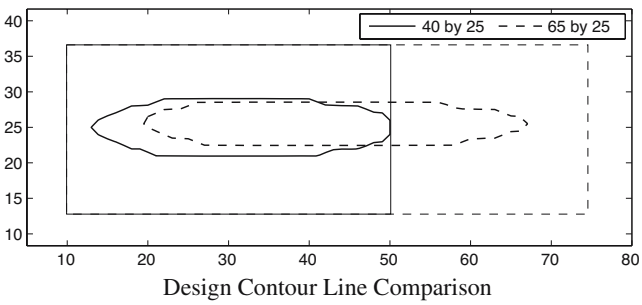

Fig. 22 Constant lattice size/increased design domain)

Table 7 Comparison of optimization results for different design domain sizes at Re = 100

Lattice size	Design domain size	Final objective
100 × 50	40 × 25	0.0098326583
100 × 50	65 × 25	0.0091845327

The objective values are the merit function values returned by SNOPT.

4.4.5 Constant lattice size/increased design domain

Figure 22 and Table 7 show the effect of an increased design domain on the design for a 100 × 50 lattice. It can be clearly seen that for the elongated design domain in Fig. 22, the design is longer and thinner than for the original design domain. This is expected due to the used objective function. As mentioned previously, at increasing Reynolds numbers, pressure drag produces the dominating forces on an object, thus it is advantageous to generate more streamlined bodies with reduced cross sections normal to the direction of flow. Whereas the short domain restricts the elongation of the optimal design, leading to a design that is pushed against the boundary of the design domain, the larger design domain provides for an enlarged design space from which the optimal solution is selected. As Table 7 shows, this leads to an improvement of the objective function value. Thus, one should be aware that the choice of the design domain size can significantly impact the topology of the optimum design.

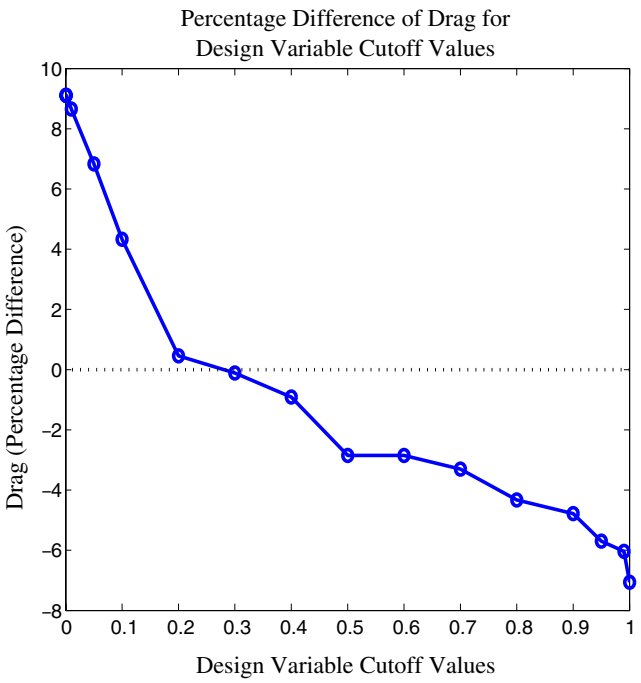

Fig. 23 Effect of the design parameter cutoff value on the drag of an optimal design at Re = 100 on a 75 × 50 lattice

4.4.6 Design convergence analysis (cutoff value analysis)

Typically all design variables converge toward their upper and lower bounds with only a small percentage of variables having intermediate values in the final design. To study the effect of the intermediate variables on the predicted performance, we set all variables to their upper or lower bounds depending on a cutoff value, meaning that if $d \leq \text{cutoff}$, $d := 0.0$, otherwise, $d := 1.0$. Varying the cutoff value, the drag of the resulting minimum drag designs for the external flow example is analyzed at Re = 100 on a 75 × 50 lattice. The results of this study are shown in Fig. 23. One can see that the design converges fairly well because the resulting drag values are within less than ±10% of the drag obtained during the optimization process for a range of $0.0001 \leq \text{cutoff} \leq 1.0$. Based on the results shown for larger lattice sizes in Fig. 18, which show a much improved geometry resolution and smoothness in the boundary region, we can conclude that the effect of the intermediate variables in the boundary region is further reduced for increased lattice sizes.

4.4.7 Comparison between lattice Boltzmann and Navier-Stokes flow solution

As the final component of the analysis of minimum drag designs for external flows, we compare the solutions obtained with the lattice Boltzmann algorithm to the flow solutions of a finite-volume-based NS solver. At this point it should be emphasized that we are comparing flow solutions of the optimal design generated with the lattice Boltzmann-based topology optimization algorithm, not solutions of separate LBM- and NS-based topology optimizations. In addition, it should be noted that top and bottom boundary conditions were modified from those shown in Fig. 13. Instead of velocity boundary conditions, slip boundary conditions were applied to simplify implementation in our NS solver. Finally, to compare the two flow solvers, we used a cutoff value of 0.5 with the LBM and used the corresponding design contour line to generate a boundary fitting mesh for the NS solver.

From Fig. 24 one can see that the corresponding velocity plots for both flow solvers are almost identical. In addition, Table 8 shows the corresponding coefficients of drag for both flow solvers, which differ by approximately 2.3%. It should be noted that at least part of this difference between the two solutions stems

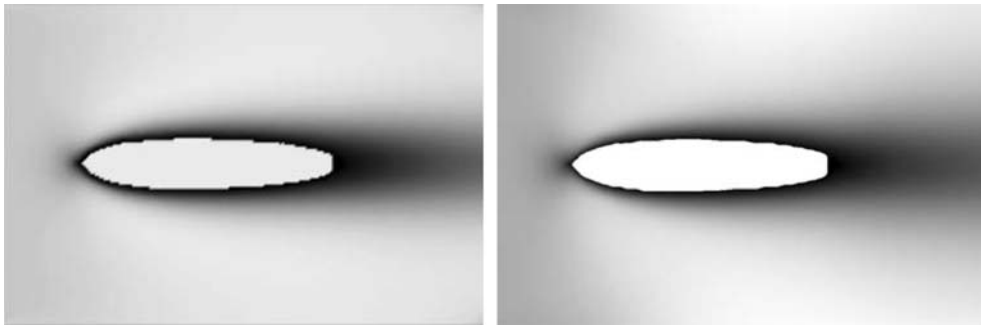

Finite Difference Lattice Boltzmann | Finite Volume Navier–Stokes

Fig. 24 Comparison between the flows obtained using the lattice Boltzmann and the finite volume methods at Re=100 on a 225 × 150 lattice

from the different meshes used. Inherently, the LBM uses an immersed boundary method leading to a stair-step type mesh, whereas the NS solver uses a body-fitted mesh. Thus, given these results, it has been shown that for low Mach number flows, the solutions obtained with the LBM compare well to those obtained with a NS flow solver.

5 Conclusions

In this first study of a formal optimization methodology and sensitivity analysis with the LBM, we have presented a novel approach to flow topology optimization. A numerical study has illustrated how the LBM can be employed to solve topology optimization problems arising in fluid mechanics. The results obtained in this study indicate that the LBM suites well for topology optimization owing to its ability to compute flows in complex geometries represented by discontinuous material distributions, ease of parallel implementation, and scalability. Furthermore, the variation of the porosity in the lattice Boltzmann formulation avoids theoretical and computational issues of varying the permeability in NS-based approaches.

While the present study renders the proposed LBM-based topology optimization method an interesting alternative to NS-based flow optimization at low Mach numbers, the efficiency of the steady-state solver and convergence problems in the optimization process need to be addressed before the methodology can be used to solve problems of practical engineering interest.

Finally, we want to emphasize that the potential of the LBM goes beyond traditional fluid mechanics because it can be used to solve fundamental transport problems, leading to a multitude of applications. To the best of the authors knowledge, the present work is the first study on integrating the LBM into a formal design optimization approach, including design sensitivity analysis.

Table 8 Comparison between the flows obtained using the lattice Boltzmann and finite volume methods at Re=100 on a 225 × 150 lattice

Flow solver	Coefficient of drag
Lattice Boltzmann	0.869771
Navier-Stokes	0.890198

Acknowledgements The authors acknowledge the support of the National Science Foundation under grant no. DMI-0348759. The opinions and conclusions presented in this study are those of the authors and do not necessarily reflect the views of the sponsoring organization.

References

Abe T (1997) Derivation of the lattice Boltzmann method by means of the discrete ordinate method for the Boltzmann equation. J Comp Physiol 131:241–246

Allaire G (1990) Homogenization of the Navier–Stokes equations in open sets perforated with tiny holes. I. Abstract framework, a volume distribution of holes. Arch Ration Mech Anal 113(3):209–259

Behrend O (1994) Solid–fluid boundaries in particle suspension simulations via the lattice Boltzmann method. Phys Rev E 51(1):1164–1175

Bendsøe MP, Sigmund O (2003) Topology optimization: theory, methods, and applications. Springer, Berlin Heidelberg New York

Bernaschi M, Succi S (2003) Accelerated lattice Boltzmann scheme for steady-state flows. Int J Mod Phys B 17(1–2):1–7

Bhatnagar PL, Gross EP, Krook M (1954) A model for collision processes in gases. I. Small amplitude processes in charged and neutral one-component systems. Phys Rev 94(3): 511–525

Borrvall T, Petersson J (2003) Topology optimization of fluids in Stokes flow. Internat J Numer Methods Fluids 41(1):77–107

Breuer M, Bernsdorf J, Zeiser T, Durst F (2000) Accurate computations of the laminar flow past a square cylinder based on two different methods: lattice-Boltzmann and finite-volume. Int J Heat Fluid Flow 21:186–196

Brinkmann HC (1947) A calculation of the viscous force exerted by a flowing fluid on a dense swarm of particles. Appl Sci Res Sect A Mech Heat 1:27
Cabuk H, Modi V (1992) Optimum plane diffusers in laminar flow. J Fluid Mech 237:373–393
Chapman S, Cowling TG (1952) The mathematical theory of nonuniform gases, 2nd edn. Cambridge University Press, London
Chen S, Doolen GD (1998) Lattice Boltzmann method for fluid flows. Annu Rev Fluid Mech 30:329–364
Dupuis A (2002) From a lattice Boltzmann model to a parallel and reusable implementation of a virtual river. Ph.D. thesis, Faculty of Sciences, University of Geneva
Evgrafov A (2005a) On the limits of porous materials in the topology optimization of Stokes flows. Appl Math Optim 52(3):263–277 doi:10.1007/s00245-005-0828-z
Evgrafov A (2005b) Topology optimization of slightly compressible fluids. ZAMM Z Angew Math Mech 86(1):46–62 doi:10.1002/zamm.200410223
Frisch U, Hasslacher B, Pomeau Y (1986) Lattice gas automata for the Navier–Stokes equation. Phys Rev Lett 56(14): 1505–1508
Frisch U, Humières D, Hasslacher B, Lallemand P, Pomeau Y, Rivet JP (1987) Lattice gas hydrodynamics in two and three dimensions. Complex Syst 1:649–707
Gersborg-Hansen A, Sigmund O, Haber R (2005) Topology optimization of channel flow problems. Struct Multidisc Optim 30(3):181–192 doi:10.1007/s00158-004-0508-7
Gill PE, Murray W, Saunders MA (2002) SNOPT: an SQP algorithm for large-scale constrained optimization. SIAM J Optim 12(4):979–1006
Gunzburger MD (2003) Perspectives in flow control and optimization. Advances in Design and Control, Society for Industrial and Applied Mathematics (SIAM), Philadelphia, PA
He X, Doolen GD (1997a) Lattice Boltzmann method on a curvilinear coordinate system: vortex shedding behind a circular cylinder. Phys Rev E 56(1):434–440
He X, Doolen GD (1997b) Lattice Boltzmann method on curvilinear coordinates system: flow around a circular cylinder. J Comput Phys 134:306–315
He X, Lou LS (1997a) A priori derivation of the lattice Boltzmann equation. Phys Rev E 55(6):6333–6336
He X, Lou LS (1997b) Theory of the lattice Boltzmann method: from the Boltzmann equation to the lattice Boltzmann equation. Phys Rev E 56(6):6811–6817
Higuera F, Jiminez J (1989) Boltzmann approach to lattice gas simulations. Europhys Lett 9(7):663–668
Higuera F, Succi S, Benzi R (1989) Lattice gas dynamics with enhanced collision. Europhys Lett 9(4):345–349
Hoekstra AG, van't Hoff J, Artoli AM, Sloot PMA (2004) Unsteady flow in a 2D elastic tube with the LBGK method. Future Gener Comput Syst 20:917–924
Hou S, Zou Q, Chen S, Doolen G, Cogley AC (1994) Simulation of cavity flow by the lattice Boltzmann method. J Comp Physiol 118:329–347
Inamuro T, Yoshino M, Ogino F (1997) Accuracy of the lattice Boltzmann method for small knudson number with finite reynolds number. Phys Fluids 9:3535–3542
Jameson A (1988) Aerodynamic design via control theory. J Sci Comput 3:233–260
Koelman JMVA (1991) A simple lattice Boltzmann scheme for Navier–Stokes fluid flow. Europhys Lett 15(6):603–607
Krafczyk M (2001) Gitter-Boltzmann-methoden: Von der theorie zur anwendung. Ph.D. thesis, Fakultät für Bauingenieur- und Vermessungswesen, Technische Universität München
Ladd AJC (1994) Numerical simulation of particular suspensions via a discrete Boltzmann equation. Part 1. Theoretical foundation. J Fluid Mech 271:285–309
Li XS, Demmel JW (2003) Superlu_dist: a scalable distributed-memory sparse direct solver for unsymmetric linear systems. ACM Trans Math Softw 29(2):110–140
Lou LS (2000) The lattice-gas and lattice Boltzmann methods: past, present, and future. In: Proceedings of the international conference on applied computational fluid dynamics,Beijing, China, 17–20 October 2000, pp. 52-83
McNamara GR, Zanetti G (1988) Use of the Boltzmann equation to simulate lattice-gas automata. Phys Rev Lett 61(20):2332–2335
Mei R, Yu D, Shyy W, Luo LS (2002) Force evaluation in the lattice Boltzmann method involving curved geometry. Phys Rev E 65(4):041, 203:1–041, 203:14
Mohammadi B, Pironneau O (2001) Applied shape optimization for fluids. Numerical mathematics and scientific computation. Oxford University Press, New York
Pironneau O (1973) On optimum profiles in Stokes flow. J Fluid Mech 59(1):117–128
Pironneau O (1974) On optimum design in fluid mechanics. J Fluid Mech 64(1):97–110
Qian YH, D'Humières D, Lallemand P (1992) Lattice BGK models for Navier–Stokes equation. Europhys Lett 17(6): 479–484
Rothman DH, Zaleski S (1994) Lattice-gas models of phase separation: interfaces, phase transitions, and multiphase flow. Rev Mod Phys 66(4):1417–1479
Spaid MAA, Phelan FR (1997) Lattice Boltzmann methods for modelling microscale flow in fibrous porous media. Phys Fluids 9(9):2468–2474
Succi S (2001) The lattice Boltzmann equation: for fluid dynamics and beyond. Numerical mathematics and scientific computation. Oxford University Press, Oxford
Svanberg K (1987) The method of moving asymptotes—a new method for structural optimization. Int J Numer Methods Eng 24(2):359–373
Wolf-Gladrow DA (2000) Lattice-gas cellular automata and lattice Boltzmann models: an introduction. Lecture notes in mathematics. Springer, Berlin Heidelberg New York
Yu D, Mei R, Shyy W (2005) Improved treatment of the open boundary in the method of lattice Boltzmann equation. Prog Comput Fluid Dyn 5(1/2):3–12